Journal of Catalysis 260 (2008) 86–92

Contents lists available at ScienceDirect

Journal of Catalysis

www.elsevier.com/locate/jcat

Oxidation of CO and H_2 by O_2 and N_2O on Au/TiO_2 catalysts in microreactors

G. Walther [a], D.J. Mowbray [a], T. Jiang [a], G. Jones [a], S. Jensen [b], U.J. Quaade [c], S. Horch [a,*]

[a] Center for Atomic-scale Materials Design (CAMD), Department of Physics, Technical University of Denmark, DK-2800 Kgs. Lyngby, Denmark
[b] Department of Micro and Nanotechnology (DTU Nanotech), Technical University of Denmark, DK-2800 Kgs. Lyngby, Denmark
[c] Center for Individual Nanoparticle Functionality (CINF), Department of Physics, Technical University of Denmark, DK-2800 Kgs. Lyngby, Denmark

ARTICLE INFO

Article history:
Received 31 July 2008
Revised 3 September 2008
Accepted 4 September 2008
Available online 1 October 2008

Keywords:
Gold
Nanoparticles
Catalysis
Microreactor
Carbon monoxide
Hydrogen
Oxygen
Nitrous oxide
Particle size
Sintering
TEM

ABSTRACT

We performed steady-state activity measurements in microreactors to obtain the reaction rates for CO and H_2 oxidation. These reactions were studied on three different gold particle sizes ($d \approx 3.6, 5.7, 16.2$ nm) using either O_2 or N_2O as oxidizing agents. From our TEM analysis, our CO oxidation rates follow the d^{-3} relationship proposed in Hvolbæk et al. [B. Hvolbæk, T.V.W. Janssens, B.S. Clausen, H. Falsig, C.H. Christensen, J.K. Nørskov, Nano Today 2 (2007) 14–18]. Density functional theory (DFT) calculations on a Au{532} surface and a Au_{12} cluster, which model corner sites, reproduced the apparent activation barriers of about 37 kJ mol^{-1} for CO oxidation on the smallest nanoparticles by both O_2 and N_2O. For all of the reactions studied, we found the overall activation barrier depended only on the size of the TiO_2 supported gold nanoparticle.

1. Introduction

In the past, gold was not thought to be catalytically active, and was even called “the noblest of all the metals” [1]. However, the discovery by Haruta et al. [2] that nanoparticulate gold is catalytically active for CO oxidation, has provoked an academic “gold rush.” This is evidenced by the exponential increase in gold catalysis publications since the early 1990s [3–6].

Many different experimental studies have been performed to understand gold's activity for CO oxidation. These investigations considered changes of the particle's morphology [7,8], a structure–activity relationship [9–11], the activity of unsupported nanoporous bulk gold [12,13], and the influence of the support on the activity [14]. CO oxidation has also been thoroughly studied theoretically using density functional theory (DFT) [1,6,15–19]. Besides CO oxidation, many other reactions have been studied on gold catalysts. These include the oxidation of hydrocarbons [5,20–24] and oxygen-containing hydrocarbons [3–5,21,25] as well as the catalytic hydrogenation of organic compounds [4,5,26].

In particular, CH_4 oxidation includes in the tail of its oxidation pathway CO oxidation and H_2 oxidation, since it only forms CO_2 and H_2 on gold catalysts [27]. Since there is a keen interest in converting CH_4 into more valuable monocarbon chemicals, it is necessary to first identify both the reaction pathway and active sites for CO and H_2 oxidation by different oxidizing agents.

The reason for this surprising activity is still under debate. After the pioneering work of Haruta [28], the activity of gold has been linked to several different effects. These include quantum-size effects [9], support-induced strain [15], charge transfer from the small gold particles to adsorbed O_2 [29] and the role of low-coordinated gold atoms [6,15,17–19].

It has recently been demonstrated that the CO oxidation activity of gold nanoparticles is inversely proportional to the cube of the average particle size ($\sim d^{-3}$), independent of the support material used [30]. This suggests that it is the corner sites which are the most active for CO oxidation by O_2.

The common oxidizing agent for CO oxidation, used in all the above studies was O_2. Very few studies deal with other oxidation agents, such as N_2O, and they focus on the decomposition and reduction of N_2O [31]. Since N_2O is known to readily dissociate into adsorbed atomic O and gas phase N_2 in the presence of CO, the oxidation of CO by N_2O involves atomic O. On the other hand, CO oxidation using O_2 has been shown to also occur via an alternative pathway, which does not include O_2 dissociation [16,32]. By using these two different oxidizing agents, we may experimentally

* Corresponding author.
E-mail address: horch@fysik.dtu.dk (S. Horch).

0021-9517/$ – see front matter
doi:10.1016/j.jcat.2008.09.003

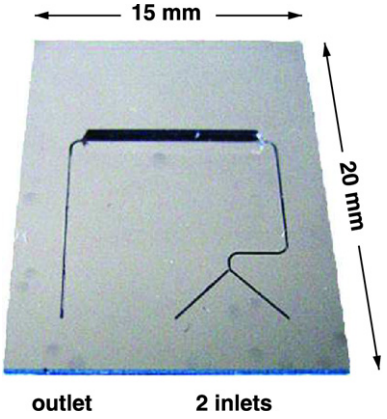

Fig. 1. Unloaded microreactor, based on silicon, with two inlets to mix gases on the chip, a (8.0 × 1.5 × 0.2) mm^3 reactor chamber and a single outlet.

compare Au nanoparticle activity for two different CO oxidation pathways.

In the present contribution, we compare the reaction rates for CO and H_2 oxidation on three different particle sizes using either O_2 or N_2O as the oxidizing agent. To corroborate our experimental findings, we also modeled the CO oxidation turnover frequency using DFT calculations on the Au{532} surface and Au_{12} cluster in a microkinetic model. Our findings suggest that such a model quantitatively describes the kinetics of CO oxidation using small Au nanoparticles ($d \lesssim 5$ nm).

2. Methods

2.1. Experimental equipment

All experiments were performed in microreactors, based on deep reactive ion-etched (DRIE) silicon wafers. Details of the fabrication process are provided in Ref. [33]. Fig. 1 illustrates the 280 μm deep capillary system that allows mixing of undiluted gases on the chip, without any danger of explosion. The dimensions of the reactor chamber are (8.0 × 1.5 × 0.2) mm^3. The whole device measures 20 mm × 15 mm × 0.35 mm and is sealed with a Viton sheet. The inlet and outlet holes are sealed with Viton O-rings to a heatable interface block that connects the external tubing to the microreactor. The temperature was measured with a K-type thermocouple and controlled using a PID-controller (Eurotherm). The gas flow was controlled by mass flow controllers (Bronkhorst), operating in the range from 0.02 to 1.00 ml min^{-1} with a precision of 0.02 ml min^{-1} at 1 bar.

The reaction products were analyzed using an Agilent gas chromatograph (3000A microGC). The GC has combined columns of 10 m molecular sieve and 3 m PLOT U with 1.0 μl back-flushing, which allows simultaneous analysis of H_2, O_2, N_2, CO, CO_2, H_2O and N_2O by a thermal conductivity detector (TCD). To avoid condensation of water, formed by the catalytic reaction of H_2, the tubing between the microreactor and the GC was kept at 100 °C, whereas the capillary of the GC itself was kept at 90 °C.

The catalysts used were 2.0 nm Au particles supported on TiO_2 (AURO*lite*™, supported by AuTEK [34]), 3.3 nm Au particles supported on TiO_2 powder (reference catalyst, supplied by the World Gold Council [35]), and 5.0 nm Au particles on TiO_2, which we shall denote as Catalysts A, B, and C, respectively. Catalysts A and B were both supported on TiO_2 P25, as stated by the suppliers.

However, Catalyst C was prepared by deposition–precipitation of unconjugated gold colloids (Ted Pella, Inc.) on anatase TiO_2 powder (Millennium Inorganic Chemicals) with an average BET area of 150–300, according to the supplier. For ease of comparison, the gold concentration of the in-house catalysts was carefully adjusted to those of the commercially available samples. The preparation was performed below 50 °C to evaporate the solvent. After the catalyst had been dried, it was calcined at 200 °C.

2.2. Catalytic reactions

We studied two different reactions on the three different gold catalysts listed above, using the two different oxidizing agents O_2 (3.5N) and N_2O (2.5N). The overall reactions and heats of formation ΔH^0 [36] are then

$$CO + N_2O \rightarrow CO_2 + N_2, \quad \Delta H^0 \approx -200.9\ \text{kJ mol}^{-1}, \tag{R1}$$

$$CO + \tfrac{1}{2}O_2 \rightarrow CO_2, \quad \Delta H^0 \approx -283.0\ \text{kJ mol}^{-1}, \tag{R2}$$

$$H_2 + N_2O \rightarrow H_2O + N_2, \quad \Delta H^0 \approx -159.8\ \text{kJ mol}^{-1}, \tag{R3}$$

$$H_2 + \tfrac{1}{2}O_2 \rightarrow H_2O, \quad \Delta H^0 \approx -241.8\ \text{kJ mol}^{-1}. \tag{R4}$$

Due to the high sensitivity of the GC to H_2, the reactants in (R4) and (R3) were diluted with 50% argon with the total flow kept constant at 1.00 ml min^{-1} for all reactions.

To minimize the contribution of self-heating of the catalyst during an exothermic reaction, all experiments were performed with a maximum of 10% conversion, except for CO oxidation where 15% was achieved at 60 °C on Catalyst A and more than 40% at 80 °C on Catalyst B. The greatest amount of heat liberated during the reactions was 26.0 mW.

To ensure reproducibility, we followed the following scheme for all measurements. First, all catalysts were activated. Catalysts B and C, containing the larger particles, were pretreated over 20 h at 80 °C to ensure steady-state activity measurements. On the other hand, due to its high activity and the possibility of sintering, Catalyst A was pretreated for 20 h at 50 °C. These pretreatments were done under stoichiometrically supplied CO and O_2, for the reaction $CO + \frac{1}{2}O_2 \rightarrow CO_2$, and a total gas flow of 1.00 ml min^{-1}. The CO conversion decreased by 33%, 17%, and 5% before stabilizing for the powder Catalysts A, B, and C, respectively. Temperature programmed activity measurements were then performed in the following sequence of reactions for each catalyst: (R2), (R1), (R3), (R4), (R2), (R1).

Since the maximum temperature reached under these reactions (120 °C on Catalyst B and 160 °C on Catalyst C) was higher than the temperature of the pretreatment (80 °C), the last two steps (remeasurement of (R2) and (R1)) were performed to ensure that the catalysts had not changed during the preceding reactions. Furthermore, to exclude any influence of the applied gases (by e.g. catalyst reduction), the reaction sequence was also conducted in reversed order—starting with (R2)—on a fresh and deactivated catalyst from the same batch. Hereby, the rate differed for each of the reactions (R1)–(R4) studied, but the proportions between (R2) and (R1), and between (R4) and (R3) were similar.

2.3. Particle analysis

Transmission electron microscopy (TEM) was used to study changes in size of the gold particles. For each catalyst, specimens were taken as the catalysts were supplied, after the pretreatment and after measurements of all four catalytic reactions. The specimens were then prepared on a carbon TEM grid by dropping a suspension of catalyst in ethanol on the grid. These were analyzed using a JEOL 3000F field emission electron microscope, which was operated at 300 kV with a LaB_6 filament as an electron source.

2.4. Theoretical methodology

All theoretical results have been obtained using the DFT code DACAPO [37]. The Kohn–Sham one-electron valence states were expanded in a plane wave basis set with a 340 eV (25 Ry) kinetic

Table 1
Activation barriers E_a and adsorption energies E_{ads} in kJ mol^{-1} for CO and H_2 oxidation by N_2O and O_2.

E (kJ mol^{-1})	Au{532} surface	Au_{12} cluster
$E_{ads}[O_2]$	−27.0	−60.8[a]
$E_{ads}[CO]$	−74.3	−91.7[a]
$E_{ads}[N_2O]$	−7.7[b]	−7.7[b]
$E_a[CO + O_2 \rightarrow CO_2 + O]$	–	27.0[a]
$E_a[CO + O \rightarrow CO_2]$	27.0	–

[a] Ref. [30].
[b] Ref. [43].

energy cutoff, and a density cutoff of 680 eV (50 Ry). The core electrons were described by Vanderbilt type ultrasoft pseudopotentials [38]. The exchange-correlation potential was described using the RPBE generalized gradient approximation self-consistently [39]. For the Au{532} surface, a $4 \times 4 \times 1$ Monkhorst–Pack **k**-point sampling was applied in the irreducible Brillouin zone. The surface was modeled by a 1×1-{532} unit cell containing 24 Au atoms with periodic boundary conditions, which corresponds to three close-packed layers. The top most layer and the adsorbents were allowed to fully relax. The O_2 adsorption energy was calculated relative to the experimentally obtained formation energy of H_2O from O_2 and H_2 [40]. This avoids difficulties associated with a DFT treatment of the O_2 triplet state in the gas phase [41].

Thermodynamic analysis was carried out using the total energies obtained from the DFT calculations. It is then possible to obtain free energies by augmenting the DFT total energies with the thermodynamics of a classical ideal gas [42]. For a gas-phase species X at temperature T and pressure p, the Gibbs free energy $G_X(p, T)$ is given by

$$G_X(p, T) = E_X + E_{ZPE} + \Delta H(T) - TS(T) + RT \ln(p/p_0), \tag{1}$$

where E_{ZPE} is the zero point energy, $\Delta H(T)$ denotes the enthalpy change due to raising the temperature from 0 K to T, $S(T)$ is the entropy at T, R is the universal gas constant, and p_0 denotes the standard pressure (taken to be 1 bar).

The potential energy of an adsorbed species X*, E_X, is given by $E_{*/X^*} - E_*$, where E_* is the energy of the clean surface and E_{*/X^*} is the energy of the adsorbate and the surface system. In order to calculate the free energy of this species, we neglect the pressure term, so that the enthalpy change is replaced by the change in internal energy. This leads to the following expression for the free energy $G_X(p, T)$:

$$G_X(p, T) = E_{X^*} + E_{ZPE} + \Delta U(T) - TS(T). \tag{2}$$

The forward rate constant for a reaction i may then be expressed in terms of the Gibb's free energies as $k_i = \nu_i \exp[-\Delta G/RT]$, where $\Delta G = \sum_{X\in\mathcal{P}} G_X - \sum_{X\in\mathcal{R}} G_X$ is the difference of the total Gibb's free energy of the products $\mathcal{P}$ and reactants $\mathcal{R}$ for reaction i, and R is the universal gas constant. The pre-exponential factor in units of s^{-1} is $\nu_i \equiv k_B T/h$, where k_B is Boltzmann's constant.

The DFT energies for the adsorbed species E_{X^*} as well as the activation barriers are given in Table 1. For the N_2O adsorption energy, we have used the experimental value given in Ref. [43].

2.5. Microkinetic model

Using the notation of Ref. [44], we may express any heterogeneous catalysis reaction in the form

$$R(g) \xrightarrow{*} P(g), \tag{R5}$$

where R(g) denotes the gas phase reactants, "*" the active sites on the catalyst, and P(g) the products in the gas phase. If we assume a Langmuir–Hinshelwood mechanism for the reaction kinetics, we may write the elementary steps in the form

$$X(g) + * \rightleftarrows X^*, \quad \forall X \in \mathcal{R}, \tag{R5a}$$

$$R^* \xrightarrow{rds} P(g) + *. \tag{R5b}$$

The turnover frequency for the rate determining step (rds) is then

$$f_{rds} \approx k^+_{rds} \prod_{X\in\mathcal{R}} \Theta_{X^*}, \tag{3}$$

where Θ_{X^*} is the fractional coverage of species X on site "*", and k^+_{rds} is the rate constant for the forward rate, which we assume dominates the total reaction rate.

Assuming the difference in zero point energies of the products and the reactants ΔE_{ZPE} is much smaller than the activation barrier E_a[rds], and the entropy of the adsorbed species is much smaller than that of the species in gas phase, $S_{X^*} \ll S_{X(g)}$, we may express the forward rate constant for the rds as

$$k^+_{rds} \approx \frac{k_B T}{h} \exp\left[-\frac{E_a[\text{rds}] - T\sum_{X\in\mathcal{P}} S_{X(g)}}{RT}\right]. \tag{4}$$

Since the adsorption steps are assumed to occur in equilibrium, the net rate

$$r_{X^*} = k^+_{X^*} p_X \Theta_* - k^-_{X^*} \Theta_{X^*} = 0, \tag{5}$$

so that

$$\Theta_{X^*} = \frac{k^+_{X^*}}{k^-_{X^*}} p_X \Theta_* = K_{X^*} p_X \Theta_*, \tag{6}$$

where p_X is the gas phase pressure of species X, while K_{X^*} is the ratio of the forward to backward rate constants. This may be expressed explicitly in terms of the adsorption energy E_{ads}[X] and gas phase entropy $S_{X(g)}$ of species X as

$$K_{X^*} \approx \exp\left[-\frac{E_{ads}[X] + TS_{X(g)}}{RT}\right], \tag{7}$$

where we again assume $S_{X^*} \ll S_X$ and ΔE_{ZPE} is much smaller than the adsorption energy of species X.

3. Results

3.1. Preliminary investigations

We shall first focus on the thermodynamically unstable N_2O, when it is applied to the catalyst and to the bare support material only. At temperatures below 160 °C no dissociation of N_2O could be measured on either Catalyst B, Catalyst C or bare TiO_2 (Degussa P25). However, in the presence of a reducing agent, e.g. H_2 or CO, N_2O could be reduced over the catalysts, but not over the bare support material [31].

Additionally, CO and O_2 were applied to bare TiO_2 in a stoichiometric ratio of 2:1 to check whether (R2) proceeds on the bare support. This was not the case.

3.2. TEM investigation on changes in particle size

Prior to discussing individual reactions, we will first analyze TEM images of the catalysts (cf. Fig. 2) to evaluate the influence of pretreatment and catalytic reactions on the gold particles. Numerical values for the change in particle size of each catalyst are summarized in Table 2.

The TEM images in Fig. 2a show typical images of Catalyst A from its state as supplied (i), its state after the pretreatment (ii)

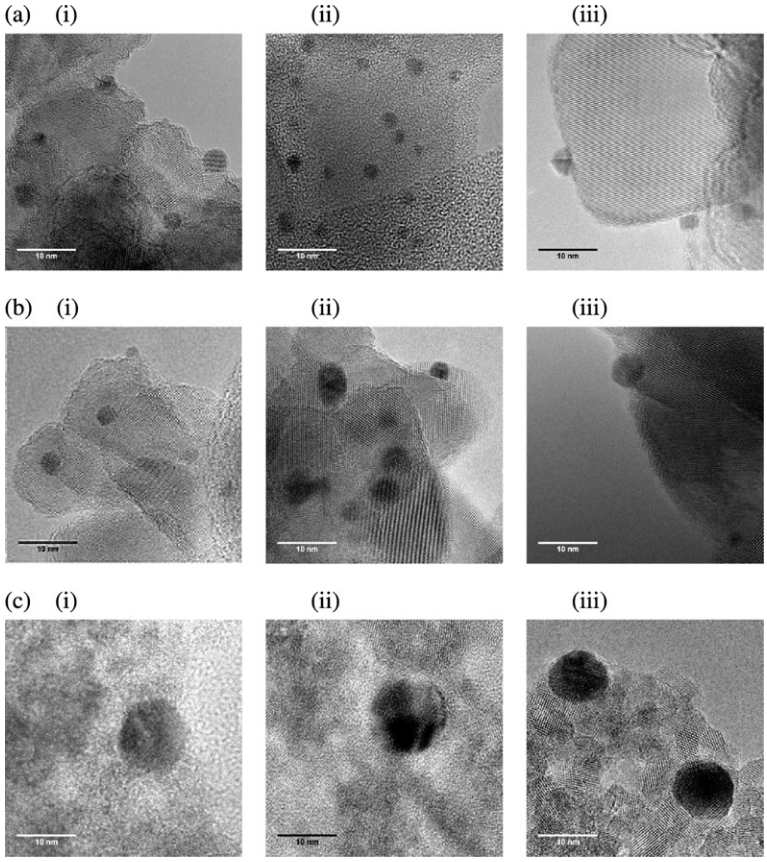

Fig. 2. Bright field TEM images of TiO_2 supported gold particles of Catalyst A (a), Catalyst B (b) and Catalyst C (c), as they were supplied/prepared (i), after the pretreatment (ii) and after catalytic reactions (iii). A summary of the change in particle size may be found in Table 2. The scale bars correspond to 10 nm in each image.

Table 2
Average TiO_2 supported gold particle size d in nm, as determined by TEM, before and after performing oxidation reactions.

d_{Au} (nm)	Gold concentration	Total gold loading	As supplied† or prepared‡	Before reaction	After reaction
Catalyst A	1.02 wt%	62.22 μg	$2.3 \pm 0.6^{\dagger}$	2.6 ± 0.6	3.6 ± 0.8
Catalyst B	1.56 wt%	63.96 μg	$3.4 \pm 0.8^{\dagger}$	3.8 ± 1.1	5.7 ± 3.4
Catalyst C	1.60 wt%	54.00 μg	$13.3 \pm 6.5^{\ddagger}$	16.2 ± 6.6	16.2 ± 6.6

and its state after catalytic reactions (iii). The particles may potentially sinter during storage. However, this was not the case, since the average of the particle size in (a) (2.3 ± 0.6 nm), based on TEM images of 97 particles, is consistent with that stated by the supplier (2.0 nm). The particles appear predominately in a truncated cuboctahedron shape. Following the pretreatment, the average particle size was determined to be 2.6 ± 0.6 nm. The particles themselves were still well dispersed on the support, as can be seen in Fig. 2a(ii). Following the catalytic reactions, the gold particles were sintered to 3.6 ± 0.8 nm.

The size of the gold particles from Catalyst B stated by the supplier (3.3 nm), was also confirmed, as may be seen in Fig. 2b(i). Fig. 2b(ii) shows the particles observed after pretreatment, which were only slightly larger. However, after reactions the gold particles' size increased significantly, cf. Fig. 2b(iii).

Fig. 2c shows Catalyst C, which was formed in-house. Already during preparation, the gold particles sintered from 5.0 nm, as supplied in solution, to 13.3 ± 6.5 nm and formed truncated cuboctahedrons. The pretreatment led to further sintering, with the average particle size becoming 16.2 ± 6.6 nm. This catalyst did not show any further changes in size after catalytic reactions.

Table 3
Apparent activation energies in kJ mol^{-1} for CO and H_2 oxidation by O_2 and N_2O, with an uncertainty of ± 2 kJ mol^{-1}.

E_a (kJ mol^{-1})	Catalyst A	Catalyst B	Catalyst C
$CO + \frac{1}{2}O_2$	36 (36.4)	38	60
$CO + N_2O$	37 (37.5)	40	60
$H_2 + \frac{1}{2}O_2$	38	38	61
$H_2 + N_2O$	39	40	60

Note. Theoretical values obtained using the microkinetic model in the low temperature regime are also provided in parentheses for Catalyst A.

3.3. Steady-state activity measurements

Fig. 3a shows Arrhenius plots for (R1)–(R4) on Catalyst A. Surprisingly, the activation energies obtained were all approximately 37 kJ mol^{-1}, as may be seen from the parallel linear fits. Table 3 summarizes these and the following activation energies. However, for CO oxidation the reaction rate differs by a factor of 2.7, when comparing the different oxidation agents with each other. For H_2 oxidation, the catalyst behaves similarly. The linear fits run parallel and the reaction rate differs by 3.2. On the Au particles of Catalyst B, which were sintered to 5.7 nm, the trend depicted on Catalyst A continues, but is even more distinct, as shown in Fig. 3b. There is approximately one order of magnitude between the rates of CO oxidation and for H_2 oxidation, using N_2O and O_2, respectively.

For CO oxidation by O_2 on Catalyst B, the reaction rate was found to reach a maximum at about 80 °C, cf. Fig. 3b. One reason for this may be that the catalyst was operated under mass-transport controlled conditions, e.g. when too little active material has been used. On the other hand, this may also be due to CO or O_2 desorption. Despite this, the parallel running fits of the

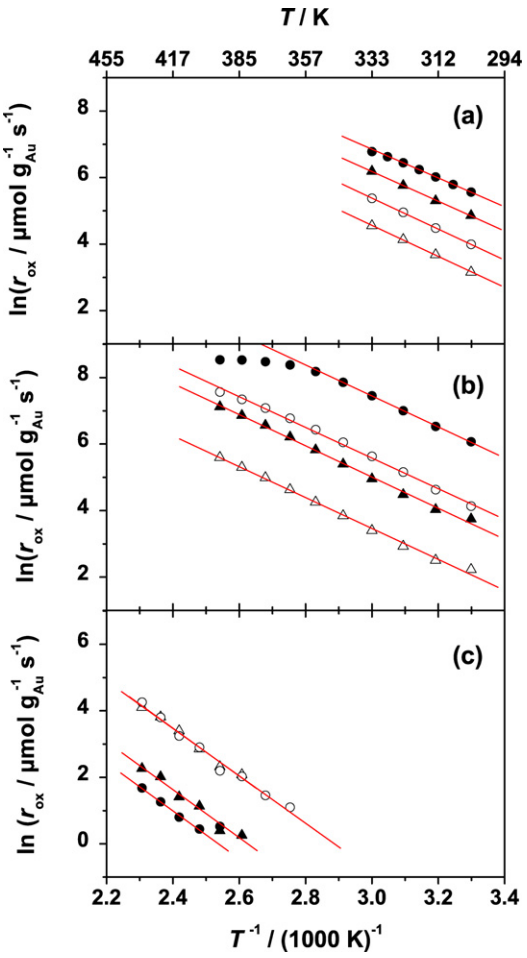

Fig. 3. Arrhenius plots of the activation energies for the four reactions on TiO_2 supported gold particles of Catalyst A (a), Catalyst B (b) and Catalyst C (c): $CO + \frac{1}{2}O_2$ (●), $CO + N_2O$ (▲), $H_2 + \frac{1}{2}O_2$ (○) and $H_2 + N_2O$ (△). An overview of the activation energies is given in Table 3.

Arrhenius plots again indicate similar activation energies around 39 kJ mol^{-1}, as shown in Table 3. These two catalysts where active even at room temperature, although O_2 was a significantly better oxidizing agent. For (R1), N_2 released from N_2O could be balanced with the CO_2 formed, indicating that the CO_2 does not originate from other sources.

Fig. 3c shows Arrhenius plots for Catalyst C and demonstrates that on this catalyst N_2O is the better oxidizing agent for CO, whereas no difference in rate could be found for H_2 oxidation. A very similar apparent activation energy of about 60 kJ mol^{-1} was again found for all the four studied reactions. On these large particles an onset of conversion could not be observed below 80 °C.

3.4. Theoretical results

It has recently been shown that for small Au nanoparticles ($d \lesssim 5$ nm) at 273 K, experimentally obtained CO oxidation rates follow a d^{-3} relationship, independent of the support material used [6,11,19]. This strongly suggests that corner sites are the active sites on small gold nanoparticles, in agreement with recent DFT studies [11,18]. By extrapolating the linear fit of our CO oxidation rate measurements for Catalyst A to 273 K, cf. Fig. 3a, we find an estimated reaction rate of approximately 66 µmol g^{-1} s^{-1} for $d \approx 3.6$ nm. This agrees well with the d^{-3} relationship of Nørskov et al. [6], where a fit to data from over 60 different sources on five different supports is presented. This is not altogether surprising, since this fit was generated by assuming the gold nanoparticle shape is the top half of a regular cuboctahedron, as is the case for our catalysts cf. Fig. 2.

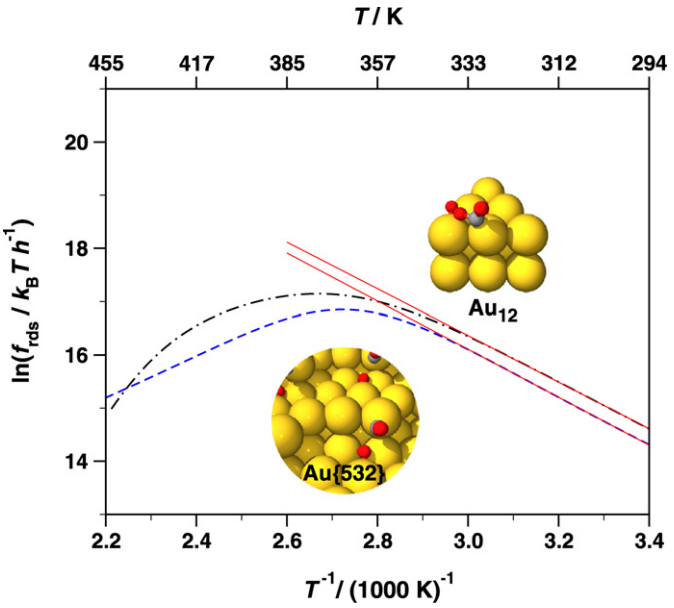

Fig. 4. Arrhenius plot of the rds turnover frequency f_{rds} in $k_BT/h \approx 10^{13}$ s^{-1} for CO oxidation by N_2O on Au{532} (blue dashed line) and by O_2 on a Au_{12} cluster (black dash-dotted line) as obtained from the microkinetic model using the DFT transition state structures depicted above [30]. The apparent activation barriers (red solid lines) in the low temperature regime ($T < 350$ K) are shown for ease of comparison with Fig. 3, and listed in Table 1.

On the other hand, the reactivity of the Au–TiO_2 interface introduces a d^{-2} correction term to the reaction rate, which becomes important for larger gold nanoparticles similar to Catalyst C. However, due to the computational complexity of properly treating the Au–TiO_2 interface for large nanoparticles, we shall restrict consideration to reactions which occur on the corner sites of the Au particles.

We begin by first considering CO oxidation using N_2O. It has been generally accepted that the reaction kinetics for CO oxidation over a metal surface follow the Langmuir–Hinshelwood mechanism. According to this, the elementary steps of adsorption and desorption are in equilibrium, and (R1) may be written in terms of the following elementary steps:

$$CO(g) + {}^{*} \rightleftarrows CO^{*}, \tag{R1a}$$

$$N_2O(g) + {}^{\diamond} \rightleftarrows N_2O^{\diamond}, \tag{R1b}$$

$$CO^{*} + N_2O^{\diamond} \overset{\text{rds}}{\rightarrow} CO_2(g) + N_2(g) + {}^{*} + {}^{\diamond}. \tag{R1c}$$

Here we have assumed that CO and N_2O adsorb on different corner sites, denoted by "*" and "◇" respectively. This is clearly the case for CO oxidation, as may be seen from the transition states depicted in the insets of Fig. 4.

Since we found N_2O does not dissociate spontaneously on gold, as has also been reported by Gluhoi et al. [31], we assume this reaction requires adsorbed CO* as a reducing agent. However, the overall barrier for (R1c) should still be the same as for CO oxidation with atomic O. On the other hand, the desorption of both N_2 and CO_2 should occur spontaneously.

To model the corner sites of a gold nanoparticle for reaction (R1c), we have chosen a Au{532} surface, which consists of both B5 and kink sites. This allows atomic O to adsorb on the preferred B5 sites while CO adsorbs on the kink sites. This is depicted in the Au{532} transition state for (R1c), shown in the lower inset of Fig. 4. Since the Au_{12} cluster model of a corner site [30] does not include B5 sites for atomic O adsorption, it yields an activation

barrier for (R1c) twice that found for the Au{532} surface. For this reason, the Au_{12} model should not be used to model (R1c).

Employing the microkinetic model described above, the turnover frequency for the rate determining step (rds) f_{rds} in s^{-1}, may then be approximated by

$$f_{rds} \approx \frac{k_B T}{h} \frac{K_{CO^*} K_{N_2O^*} p_{CO} p_{N_2O}}{(1 + K_{CO^*} p_{CO})(1 + K_{N_2O^*} p_{N_2O})} \times \exp\left[-\frac{E_a[\text{rds}] - T(S_{CO_2(g)} + S_{N_2(g)})}{RT} \right], \quad (8)$$

where K_{CO^*} and $K_{N_2O^*}$ are given in (7). The required activation and adsorption energies for the Au{532} surface are provided in Table 1 and the temperature dependent gas phase entropies are interpolated using data from Ref. [36].

Fig. 4 shows the temperature dependence of the turnover frequency f_{rds}, for the rds of CO oxidation by N_2O on Au{532}. We found f_{rds} follows an Arrhenius-like behavior in the low temperature regime ($T < 350$ K). However, at higher temperatures the turnover frequency decreases with increasing temperature, with an apex at $T \approx 360$ K.

When using O_2 instead of N_2O to oxidize CO, we may again assume a Langmuir–Hinshelwood mechanism, so that the elementary steps for (R2) may be written as

$$CO(g) + {}^* \rightleftarrows CO^*, \quad (R2a)$$

$$O_2(g) + {}^{\diamond} \rightleftarrows O_2^{\diamond}, \quad (R2b)$$

$$CO^* + O_2^{\diamond} \xrightarrow{\text{rds}} CO_2^* + O^{\diamond}, \quad (R2c)$$

$$CO^* + O^{\diamond} \Rightarrow CO_2(g) + {}^* + {}^{\diamond}, \quad (R2d)$$

where "*" and "◇" denote active sites for CO and O_2 respectively, on the Au particle.

Since O_2 is known not to dissociate spontaneously on gold nanoparticles [45], we assume CO is oxidized directly by O_2 (R2c), as discussed in Refs. [30,46]. We further assume (R2c) is the rate determining step, so that (R2d) occurs relatively quickly. This is justified in the case of high CO coverages, since CO_2 will quickly desorb from the surface.

To model the gold nanoparticle corner sites for reaction (R2c), we have used the Au_{12} cluster model described in Ref. [30]. As seen in Table 1, such a model yields much higher adsorption energies, particularly for O_2. This is necessary to correctly model (R2c) on gold nanoparticles. As shown in the upper inset of Fig. 4, the transition state for (R2d) on the Au_{12} cluster model has the O_2 molecule strongly adsorbed on the corner site, while CO is adsorbed on the edge.

Again employing our microkinetic model, f_{rds} for (R2) may be approximated by

$$f_{rds} \approx \frac{k_B T}{h} \frac{K_{O_2^{\diamond}} K_{CO^*} p_{O_2} p_{CO}}{(1 + K_{O_2^{\diamond}} p_{O_2})(1 + K_{CO^*} p_{CO})} \times \exp\left[-\frac{E_a[\text{rds}] - T S_{CO_2(g)}}{RT} \right], \quad (9)$$

where K_{CO^*} and $K_{O_2^{\diamond}}$ are given in (7). The necessary activation and adsorption energies for the Au_{12} cluster model are provided in Table 1 and the temperature dependent gas phase entropies are interpolated using data from Ref. [36].

The temperature dependence of f_{rds} for CO oxidation by O_2 on Au_{12} is shown in Fig. 4. We again found f_{rds} has an Arrhenius behavior in the low temperature regime ($T < 350$ K). As with N_2O, we found at higher temperatures the turnover frequency decreases with increasing temperature, with an apex at $T \approx 370$ K.

4. Discussion

Table 3 shows the overall trend in apparent activation energies for the reactions measured on Catalysts A, B and C. First, there is a clear size dependence trend from large gold particles with less reactivity to the significantly more reactive smaller ones for all the reactions studied. Second, there is very little difference in the apparent overall activation barrier for CO or H_2 oxidation, irrespective of the oxidizing agent used. This is seen for both experimental and theoretical apparent activation barriers, which are in quantitative agreement for Catalyst A ($d \lesssim 5$ nm), in the low temperature regime ($T < 350$ K), as shown in Table 3. However, there is little correlation between the experimental reaction rate and theoretical turnover frequency for the larger Catalyst C. This may be expected, as for larger Au nanoparticles ($d \gtrsim 10$ nm), the bulk gold properties may begin to dominate, so that a cluster-based theoretical model is no longer applicable.

Clearly it would be desirable to get a direct comparison between measured rates and calculated turnover frequencies. However, such a comparison requires atomic resolution characterization of the particles in question. Given the large dispersity in particle size for our catalysts we are unable to provide such experimental detail. However, it should be born in mind that the trends for the theoretical turnover frequency should match those of the experimental rate, as shown in Table 3.

We shall first focus on CO oxidation using N_2O according to (R1). From the preliminary investigations it may be concluded that in the absence of a reducing agent, the dissociation of N_2O is inhibited. This may be accounted for by the very weak Au–N_2O bond which leads to rapid desorption of N_2O [31]. However, this reaction changes the overall entropy of the system only slightly, since one diatomic and one triatomic species both adsorb and desorb from the surface in (R1). This means that although there is only a small N_2O coverage, for high CO coverage experiments the reaction rate should be significant. On the other hand, as seen in Fig. 4, at higher temperatures ($T > 350$ K) CO begins to desorb from the surface and the turnover frequency begins to decrease at higher temperatures ($T > 360$ K). We were unable to verify this experimentally since we found gold particle sintering began to occur in this temperature range, as shall be discussed later.

For the case of CO oxidation by O_2 according to (R2), there is a significant loss of entropy in the overall reaction, as three diatomic species adsorb, but two triatomic species desorb. Thus a high O_2 adsorption energy is required for the reaction rate to be significant. As this is the case for small gold nanoparticles and the Au_{12} cluster model for a corner site, we employ this model for (R2). Even so, we find at higher temperatures ($T > 370$ K) the reaction rate decreases significantly as both O_2 and CO begin to desorb from the gold nanoparticle. This may be seen in the reaction rate plots for CO oxidation by O_2 on Catalyst B, shown in Fig. 3. Here, the reaction rate begins to flatten at about 370 K, in agreement with the theoretical turnover frequency shown in Fig. 4.

Besides the activity, stability is the next most important property of an industrial catalyst. With a view on the gold loading of the catalysts used, noted in Table 2, it seems clear that small particles with a high loading are more likely to sinter than with lower loadings. One reason for this is that due to the low melting point of gold [47,48] or quasi-melting [49], gold particles already become mobile at only slightly elevated temperatures. The larger the particles at a constant loading are, the fewer particles are on the support, and the larger is the distance to their nearest neighbor.

Fig. 2 illustrates the sintering for different gold particle sizes during the pretreatment, when comparing image (i) with image (ii), as well as during the activity measurements. Since the activity measurements were performed in a sequence (as described above),

the change in particle size may be related to 40 °C more in heat applied than for the catalytic reactions driven on Catalyst B.

Catalyst A was not heated more than the pretreatment required. This means that the sintering on this catalyst is related only to how the reactions proceeded. Across the general observations published regarding CO oxidation on TiO_2 supported gold using O_2 as an oxidizing agent, sintering of nanoparticulate gold has not been reported. Gold nanoparticles have also been found to be a stable catalyst in the presence of H_2 and H_2O [50]. This suggests that the sintering observed on Catalyst A is related to the supply of N_2O. In contrast, the particles of Catalyst C did not significantly sinter, even though the maximum temperature was 80 °C higher than the temperature of the pretreatment.

5. Conclusions

We have investigated two different reactions on three TiO_2 supported gold catalysts with two different oxidizing agents. Experimental results for CO oxidation on Catalysts A and B agree with both our theoretical model and the literature, following the d^{-3} trend advocated by Nørskov et al. [6]. However, for Catalyst C we found more bulk-like behavior.

Based on our theoretical model, we find oxidizing CO by N_2O involves a CO–O transition state, with atomic O adsorbed on the gold B5 sites and CO on the corners. On the other hand, CO oxidation by molecular O_2 occurs via a different reaction pathway, which instead involves a meta-stable intermediate CO–O_2. In this case, O_2 is strongly adsorbed on gold corner sites while CO is adsorbed on the nearby edge sites (cf. Fig. 2).

However, although the two oxidizing agents used proceeded via *different* reaction pathways on *different* active sites, the apparent overall activation barriers obtained from both theory and experiment were found to be the *same*. From experiment, we found that H_2 and CO oxidation proceed similarly, with common activation barriers and rate enhancements when comparing oxidizing agents.

Additionally, from our TEM analysis we conclude that N_2O oxidation may promote sintering of Au nanoparticles on TiO_2, since significant sintering has not been found for CO and H_2 oxidation on gold nanoparticles using O_2 [27,50].

Acknowledgments

The authors gratefully acknowledge support in the form of catalysts provided by Project AuTEK. We also thank F.B. Grumsen for assistance with taking TEM images, and T. Bligaard for useful discussions. G. Walther and D.J. Mowbray also acknowledge financial support from NABIIT. The Center for Atomic-scale Materials Design is funded by the Lundbeck Foundation. The authors also acknowledge support from the Danish Center for Scientific Computing through grant HDW-1103-06.

References

[1] B. Hammer, J.K. Nørskov, Nature 376 (1995) 238–240.
[2] M. Haruta, T. Kobayashi, H. Sano, N. Yamada, Chem. Lett. (1987) 405–408.
[3] A.S.K. Hashmi, G.J. Hutchings, Angew. Chem. 45 (2006) 7896.
[4] G.C. Bond, D.T. Thompson, Catal. Rev. Sci. Eng. 41 (1999) 319–388.
[5] G.C. Bond, C. Louis, D.T. Thompson, Catalysis by Gold, first ed., Imperial College Press, London, 2006.
[6] B. Hvolbæk, T.V.W. Janssens, B.S. Clausen, H. Falsig, C.H. Christensen, J.K. Nørskov, Nano Today 2 (2007) 14–18.
[7] D.E. Starr, S.K. Shaikhutdinov, H.-J. Freund, Top. Catal. 36 (2005) 33–41.
[8] H.-J. Freund, Catal. Today 117 (2006) 6–17.
[9] M. Valden, X. Lai, D.W. Goodman, Science 281 (1998) 1647–1649.
[10] M.S. Chen, D.W. Goodman, Science 306 (2004) 252–255.
[11] T.V.W. Janssens, A. Carlsson, A. Puig-Molina, B.S. Clausen, J. Catal. 240 (2006) 108–113.
[12] C. Xu, J. Su, X. Xu, P. Liu, H. Zhao, F. Tian, Y. Ding, J. Am. Chem. Soc. 129 (2007) 42–43.
[13] C. Xu, X. Xu, J. Su, Y. Ding, J. Catal. 252 (2007) 243–248.
[14] R.J.H. Grisel, B.E. Nieuwenhuys, Catal. Today 64 (2001) 69–81.
[15] M. Mavrikakis, P. Stoltze, J.K. Nørskov, Catal. Lett. 64 (2000) 101–106.
[16] Z.-P. Liu, P. Hu, A. Alavi, J. Am. Chem. Soc. 124 (2002) 14770–14779.
[17] N. Lopez, J.K. Nørskov, J. Am. Chem. Soc. 124 (2002) 11262–11263.
[18] N. Lopez, T.V.W. Janssens, B.S. Clausen, Y. Xu, M. Mavrikakis, T. Bligaard, J.K. Nørskov, J. Catal. 223 (2004) 232–235.
[19] T.V.W. Janssens, B.S. Clausen, B. Hvolbæk, H. Falsig, C.H. Christensen, T. Bligaard, J.K. Nørskov, Top. Catal. 44 (2007) 15–26.
[20] B.E. Solsona, T. Garcia, C. Jones, S.H. Taylor, A.F. Carley, G.J. Hutchings, Appl. Catal. A Gen. 312 (2006) 67–76.
[21] D.T. Thompson, Top. Catal. 38 (2006) 231–240.
[22] R.D. Waters, J.J. Weimer, J.E. Smith, Catal. Lett. 30 (1994) 181–188.
[23] S. Ivanova, C. Petit, V. Pitchon, Appl. Catal. A Gen. 267 (2004) 191–201.
[24] S. Ivanova, C. Petit, V. Pitchon, Gold Bull. 39 (2006) 3–8.
[25] C.H. Christensen, B. Jorgensen, J. Rass-Hansen, K. Egeblad, R. Madsen, S.K. Klitgaard, S.M. Hansen, M.R. Hansen, H.C. Andersen, A. Riisager, Angew. Chem. 45 (2006) 4648–4651.
[26] M.-C. Daniel, D. Astruc, Chem. Rev. 104 (2004) 293–346.
[27] G. Walther, G. Jones, S. Jensen, U.J. Quaade, S. Horch, Catal. Today, in press.
[28] M. Haruta, Catal. Today 36 (1997) 153–166.
[29] J.A. van Bokhoven, C. Louis, J.T. Miller, M. Tromp, O.V. Safonova, P. Glatzel, Angew. Chem. Ger. Ed. 118 (2006) 4767–4770.
[30] H. Falsig, B. Hvolbæk, I.S. Kristensen, T. Jiang, T. Bligaard, C.H. Christensen, J.K. Nørskov, Angew. Chem. 47 (2008) 4835–4839.
[31] A.C. Gluhoi, M.A.P. Dekkers, B.E. Nieuwenhuys, J. Catal. 219 (2003) 197–205.
[32] L.M. Molina, B. Hammer, Phys. Rev. B 69 (2004) 155424.
[33] U.J. Quaade, S. Jensen, O. Hansen, J. Appl. Phys. 97 (2005) 44906.
[34] http://www.mintek.co.za.
[35] http://www.gold.org.
[36] D.R. Lide, Handbook of Chemistry and Physics, 87th ed., CRC Press, Boca Raton, 2006–2007.
[37] http://wiki.fysik.dtu.dk/dacapo.
[38] D. Vanderbilt, Phys. Rev. B 41 (1990) 7892–7895.
[39] B. Hammer, L.B. Hansen, J.K. Nørskov, Phys. Rev. B 59 (1999) 7413–7421.
[40] J.K. Nørskov, J. Rossmeisl, A. Logadottir, L. Lindqvist, J.R. Kitchin, T. Bligaard, H. Jonsson, J. Phys. Chem. B 108 (2004) 17886–17892.
[41] S. Kurth, J.P. Perdew, P. Blaha, Int. J. Quant. Chem. 75 (1999) 889–909.
[42] J.H. Noggle, Physical Chemistry, third ed., Harper Collins, New York, 1996.
[43] B.E. Nieuwenhuys, A.C. Gluhoi, E.D.L. Rienks, C.J. Weststrate, C.P. Vinod, Catal. Today 100 (2005) 49–54.
[44] M. Boudart, G. Djéga-Mariadassou, Kinetics of Heterogeneous Catalytic Reactions, Princeton University Press, Princeton, NJ, 1984.
[45] J.K. Nørskov, T. Bligaard, A. Logadottir, S. Bahn, L.B. Hansen, M. Bollinger, H. Bengaard, B. Hammer, Z. Sljivancanin, M. Mavrikakis, Y. Xu, S. Dahl, C.J.H. Jacobsen, J. Catal. 209 (2002) 275–278.
[46] L.M. Molina, B. Hammer, Appl. Catal. A Gen. 291 (2005) 21–31.
[47] P. Buffat, J.P. Borel, Phys. Rev. A 13 (1976) 2287–2298.
[48] H. Sykes, E. Charles, F.J. Williams, M.S. Tikhov, R.M. Lambert, J. Phys. Chem. B 106 (2002) 5390–5394.
[49] P.M. Ajayan, D.L. Marks, Phys. Rev. Lett. 60 (1988) 585–587.
[50] P. Landon, J. Ferguson, B.E. Solsona, T. Garcia, S. Al-Sayari, A.F. Carley, A.A. Herzing, C.J. Kiely, M. Makkee, J.A. Moulijn, A. Overweg, S.E. Golunski, G.J. Hutchings, J. Mater. Chem. 16 (2006) 199–208.